A phase-field method for simulations of two-phase flows on unstructured grids

By H. Hwang AND S. S. Jain

1. Motivation and objectives

Two-phase flows are prevalent in nature and industrial applications, for example, surface cooling (Liu *et al.* 2019), wind-wave interaction (Buckley & Veron 2016), Rayleigh–Taylor (Sharp 1984; Hwang *et al.* 2021) and Richtmyer–Meshkov (Holmes *et al.* 1999) instabilities and atomization of liquid jets (Gorokhovski & Herrmann 2008; Prakash *et al.* 2019; Hwang *et al.* 2022) and drops (Jain *et al.* 2019), and flows with phase change (Tryggvason *et al.* 2005) and a moving contact line (Sui *et al.* 2014). In such flows, computational modeling of interfaces separating two immiscible fluids is numerically challenging due to the discontinuity in quantities such as density and viscosity across the interface. To tackle this challenge, a variety of interface-capturing and interface-tracking methods have been developed. These include volume-of-fluid (VOF), level-set (LS), phase-field (PF), and front-tracking methods, as well as hybrid methods such as coupled LS and VOF and coupled PF and VOF methods (Mirjalili *et al.* 2017). Each of the methods has its own strengths in two-phase flow simulations. However, researchers are actively investigating how to minimize the artificial diffusion of interfaces, to prevent under/overshoot of volume fractions, and to conserve mass while maintaining the efficiency of the methods. Most importantly, the implementation and applicability of these methods on unstructured grids are imperative for more complex and practical two-phase engineering applications.

The VOF method has been widely used for computational simulations of interfaces since it is known to conserve mass and have advantages in handling complex interface morphology changes. The VOF method can be classified into geometric and algebraic types. Geometric VOF reconstructs the interface based on geometric representation (e.g., plane or quadratic surface), and the reconstructed segments are advected in a Lagrangian fashion (Youngs 1982; Rider & Kothe 1998). Accordingly, geometric VOF keeps sharp interfaces; however, its geometric manipulations become inherently complicated on unstructured grids. Moreover, operations related to interfaces are localized in interface cells, leading to high computational cost and parallel load imbalance (Jofre *et al.* 2015). Nevertheless, this method has been successfully extended to unstructured grids (Ivey & Moin 2015, 2017; Xie & Xiao 2017). On the other hand, the algebraic VOF method computes the face fluxes algebraically using compressive difference schemes, avoiding reconstruction of the interface and related issues (Lafaurie *et al.* 1994). Nonetheless, an issue related to the smearing of the interface persists, especially, in the region of high shear and high local Courant–Friedrichs–Lewy (CFL) number. To overcome the numerical issues of the geometric and algebraic VOF methods, the THINC (tangent of hyperbolic interface capturing) method, a hybrid geometric/algebraic approach, was proposed (Xiao *et al.* 2005; Xie & Xiao 2017). However, its application to unstructured grid adds another level of complexity (Xie & Xiao 2017). Additionally, it is reported that the phase indicator variable is not bounded (Kim *et al.* 2021; Kumar *et al.* 2021) without the use of flux limiters.

Recently, the PF method has been gaining popularity as an alternative interface-

capturing method with many attractive features. The PF method or a diffuse-interface method models the interface as a diffused layer over several cells, as the name indicates, rather than in a sharp discontinuous representation. Thus, numerical operations, such as derivatives, can be applied even across the interface, as is done in a single-phase problem, leading to high scalability of the method. Moreover, the sharpness of the interface is easily controlled by the use of an interface-regularization term. There are various PF methods in the literature, which can be classified into Cahn-Hilliard-based methods (Cahn & Hilliard 1958) and Allen-Cahn-based methods (Allen & Cahn 1979). A Cahn-Hilliard PF model is conservative but involves a fourth-order spatial derivative in the equation, which requires careful construction of the numerical methods. In contrast, an Allen-Cahn PF model does not involve fourth-order derivatives in the equation and is not conservative. A conservative version of the Allen-Cahn based model has been proposed by Chiu & Lin (2011). This model has been extended to unstructured grids in the context of a finite-element formulation by Joshi & Jaiman (2018). A flux-limiter-based diffuse-interface approach for compressible flows has been developed by Chiapolino *et al.* (2017). More recently, Jain (2022) proposed an accurate conservative diffuse-interface/phase-field (ACDI/ACPF) model and showed that this method is robust, conservative, and significantly more accurate than other PF models in the literature. Jain (2022) showed that this PF model can maintain boundedness of the volume fraction while maintaining the interface thickness on the order of only one or two grid points. The capability of this PF model to maintain such sharp interfaces without the need for any special geometric treatment, unlike the VOF method, makes it a highly attractive interface-capturing method for accurate simulation of two-phase flows at an affordable cost.

The ACDI method introduces a signed-distance-like function replacing the PF variable in the sharpening term of the interface-regularization term. Thus, the sharp gradient in the PF variable across interfaces is eliminated, yielding a more accurate computation of the sharpening flux. As a result, the ACDI method demonstrates enhanced accuracy compared to the previously reported conservative PF methods. Moreover, it improves the computation of the surface tension force, significantly reduces spurious velocity fields near interfaces, and achieves a less restrictive CFL condition. Altogether, this PF method has great potential as an accurate, cost-efficient, and highly scalable interface-capturing method for the simulation of complex interfacial flows.

The objective of the present work is to adopt the ACDI method on unstructured grids that will allow for simulations of two-phase flows in complex geometries and for large-scale practical applications in engineering. We propose an implementation of this PF model on unstructured Voronoi grids and evaluate its performance using various interface advection test cases and hydrodynamic-coupled simulations. We also design and propose new standardized test cases for the evaluation of interface-capturing methods on unstructured grids.

2. Methods

2.1. *Accurate conservative phase-field model*

We consider incompressible two-fluid flows. The volume fraction of one of the fluids is indicated by the phase-field variable $\phi = \phi_1$, which satisfies the relation $\sum_{l=1,2} \phi_l = 1$ by

definition. Then, the ACDI model for ϕ (Jain 2022) is written as

$$\frac{\partial \phi}{\partial t} + \vec{\nabla} \cdot (\vec{u}\phi) = \vec{\nabla} \cdot \left\{ \Gamma \left\{ \epsilon \vec{\nabla}\phi - \frac{1}{4}\left[1 - \tanh^2\left(\frac{\psi}{2\epsilon}\right)\right] \frac{\vec{\nabla}\psi}{|\vec{\nabla}\psi|} \right\} \right\}, \tag{2.1}$$

where $\vec{u}$ is the velocity, Γ denotes the velocity-scale parameter, and ϵ is the interface thickness scale parameter. ψ represents the signed-distance-like function from the interface, which is defined as

$$\psi = \epsilon \ln\left(\frac{\phi + \varepsilon}{1 - \phi + \varepsilon}\right). \tag{2.2}$$

Note that a small number ε is added to both the numerator and denominator to ensure the boundedness of ϕ, and ε is chosen as $\varepsilon = 10^{-100}$. The right-hand-side term of Eq. (2.1) is the interface-regularization term, which is an artificial term that is added to maintain the constant thickness of interface. The interface-regularization term contains the diffusion and sharpening terms, which balance each other to maintain a constant interface thickness on the order of ϵ.

2.2. *Navier–Stokes equations*

Addition of the regularization term in Eq. (2.1) modifies the way the volume fraction is transported. This modified transport of volume fraction should be consistently accounted for in the transport of mass, momentum, and energy (Jain 2022). If we represent the artificial regularization volume flux as $\vec{a}$,

$$\vec{a} = \Gamma \left\{ \epsilon \vec{\nabla}\phi - \frac{1}{4}\left[1 - \tanh^2\left(\frac{\psi}{2\epsilon}\right)\right] \frac{\vec{\nabla}\psi}{|\vec{\nabla}\psi|} \right\}, \tag{2.3}$$

then the implied artificial mass flux $\vec{f}$ can be written as

$$\vec{f} = \sum_{l=1}^{2} \rho_l \vec{a}_l = \left\{ (\rho_1 - \rho_2)\Gamma \left\{ \epsilon \vec{\nabla}\phi - \frac{1}{4}\left[1 - \tanh^2\left(\frac{\psi}{2\epsilon}\right)\right] \frac{\vec{\nabla}\psi}{|\vec{\nabla}\psi|} \right\} \right\}, \tag{2.4}$$

where ρ_l is the density of phase l. As a result, the mass transport equation has an additional term due to the artificial mass flux, which is written as

$$\frac{\partial \rho}{\partial t} + \frac{\partial \rho u_j}{\partial x_j} = \frac{\partial f_j}{\partial x_j}. \tag{2.5}$$

Here the density ρ is computed as $\rho = \rho_1\phi + \rho_2(1 - \phi)$.

Furthermore, the effect of the regularization term is considered in the momentum equation as

$$\frac{\partial \rho u_i}{\partial t} + \frac{\partial \rho u_i u_j}{\partial x_j} = -\frac{\partial p}{\partial x_i} + \frac{\partial \tau_{ij}}{\partial x_j} + \frac{\partial u_i f_j}{\partial x_j} + \sigma\kappa\frac{\partial \phi_1}{\partial x_i}, \tag{2.6}$$

where τ_{ij} is a shear stress, $\tau_{ij} = 2\mu S_{ij} = \mu(\partial u_i/\partial x_j + \partial u_j/\partial x_i)$, and p is the pressure. Surface tension force is introduced using the continuum-surface force formulation (Brackbill *et al.* 1992), σ is the surface tension coefficient, and κ is the surface curvature, whose definition follows $\kappa = -\vec{\nabla} \cdot \vec{n} = -\vec{\nabla} \cdot (\vec{\nabla}\psi/|\vec{\nabla}\psi|)$. The use of ψ to compute curvature in the surface tension force was shown in Jain (2022) to improve modeling of the surface tension force and reduce spurious currents.

2.3. *Voronoi grids and discretization of ACDI model*

In this work, a Voronoi mesh-based unstructured grid is adopted. The Voronoi grid divides a volume of space into regions, where each location in the region is closer to the associated seed point than to any other seed points, based on Euclidean distance. The grid is generated using the `stitch` tool, a fast Voronoi meshing package developed at Cascade Technologies (Brès *et al.* 2018), which is now part of Cadence Design Systems. This package generates a hexagonal close-packed (HCP) array of points, and the resulting mesh has a uniform 14-sided polyhedral in the regions of the domain away from the boundaries and grid transitions. Figure 1 shows a schematic of an unstructured Voronoi grid.

Some of the advantages of the Voronoi grids, compared to other unstructured grids, are as follows.

(*a*) In Voronoi grids, vertex locations uniquely define the geometric information (cell volume, face area, and normals) and the connectivity of the Voronoi mesh (neighbors of a cell). This deterministic connection between the points simplifies mesh generation and manipulation and improves mesh quality using Lloyd iteration in a robust and stable way (Ambo *et al.* 2020).

(*b*) The face normals and cell displacement vectors are orthogonal to one another by construction. This orthogonality enables computational efficiencies for both the mesh generator and the fluid solver (see Figure 1).

(*c*) Cell faces are located at the center of the cell displacement vectors (see Figure 1), which will make the Voronoi grid suitable for implementation of low-dissipative central schemes.

(*d*) Voronoi mesh generation is highly parallelizable due to its local nature, and it avoids the issue of degenerate point sets with the Delaunay triangulation (Brès *et al.* 2018).

In this work, we use a collocated grid arrangement; in other words, all the variables being solved (ϕ, ψ, ρ, u_i, and p) are stored at the Voronoi seed points. This is done to avoid the need to develop of complicated operators (Perot 2000) in an unstructured staggered grid setting.

In this study, the governing equations, Eqs. (2.1)–(2.6), are spatially discretized using a skew-symmetric-type second-order flux-split central difference scheme (Jain & Moin 2022), and a fourth-order Runge-Kutta (RK4) method is chosen as the time-integration scheme.

The right-hand-side of Eq. (2.1) is a divergence of the artificial regularization volume flux $\vec{a}$ in Eq. (2.3); thus, it is computed in a finite-volume formulation as

$$\sum_{f_k} (\vec{a}_{f_k} \cdot \vec{n}_{f_k})\, A_{f_k}, \tag{2.7}$$

where f_k indicates the cell face between the cell centroid p and that of the neighboring cell nbr_k. $\vec{n}_{f_k}$ and A_{f_k} are the unit face normal and the cell face area of f_k, respectively, as shown in Figure 1. Because the dot product in Eq. (2.7) is calculated at the cell faces, the volume flux $\vec{a}$ must be evaluated at the cell faces.

Note that ϕ and ψ are located at the seed points. To compute the diffusion flux at the cell face, the gradient of ϕ dotted with the face normal is computed, following Eq. (2.7), as

$$\sum_{f_k} \left(\vec{\nabla}\phi_{f_k} \cdot \vec{n}_{f_k}\right) A_{f_k} = \sum_{f_k} \{(\phi_{nbr_k} - \phi_p)/|\mathbf{x_p} - \mathbf{x_{nbr_k}}|\}\, A_{f_k}, \tag{2.8}$$

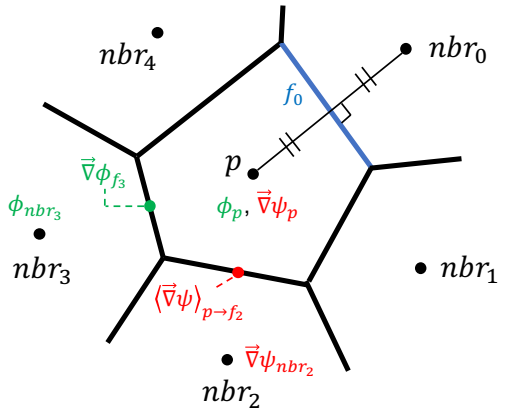

FIGURE 1. A schematic of an unstructured Voronoi grid. The black dots denote the seed points of cell p and those of its neighboring cells. The cell face and the cell displacement vector between the cell p and one of its neighbor nbr_k are indicated as f_k and $\mathbf{x_p} - \mathbf{x_{nbr_k}}$, respectively.

where $\mathbf{x_p}$ and $\mathbf{x_{nbr}}$ denote the displacement vectors of cell centroids p and nbr, respectively.

Next, we compute $\vec{\nabla}\psi$ at the seed points using the least-square gradient operator (Mahesh *et al.* 2004). The sharpening flux is computed at the cell face by cell-to-face interpolation $\langle\cdot\rangle_{p\to f_k}$, which is the midpoint value, of the gradient of ψ for the interface normal. The tanh function is computed at the cell face using cell-to-face interpolated ψ. Following the form of Eq. (2.7), the sharpening term is calculated as

$$\sum_{f_k}\left\{1-\tanh\left(\frac{\langle\psi_p\rangle_{p\to f_k}}{2\epsilon}\right)\right\}\left(\langle\vec{\nabla}\psi_p\rangle_{p\to f_k}\cdot\vec{n}_{f_k}\right)A_{f_k}. \tag{2.9}$$

2.4. *Projection method algorithm*

In this section, the projection method algorithm used in this work is presented in full detail. Although all the results shown in this work are computed using RK4, a single full time-step iteration from time step n to $n+1$ is explained in the explicit Euler framework for the sake of simplicity and clarity. In addition, we omit the viscous term for the same reason.

2.4.1. *PF variable and density update*

First, we update ϕ by solving

$$\frac{\phi_p^{n+1}-\phi_p^n}{\Delta t}V_{cv} = -\left[\sum_{f_k}\langle\phi_p\rangle_{p\to f_k}U_{f_k} - \sum_{f_k}(\vec{a}_{f_k}\cdot\vec{n}_{f_k})\right]^n A_{f_k}, \tag{2.10}$$

where the superscripts n and $n+1$ represent time-step indices, $U^n_{f_k} = (RU)^n_{f_k}/\langle\rho^n_p\rangle_{p\to f_k}$ is the face velocity, and RU is the mass flux computed using Eq. (2.11) at the previous timestep/substep, which satisfies the divergence-free condition. V_{cv} and A_{f_k} are cell volume and face area, respectively. Then, the density in the next time step is updated using $\rho^{n+1} = \rho_1\phi + \rho_2(1-\phi)$.

2.4.2. *Momentum equation update*

We advance the momentum equation to compute the intermediate $\rho^{n+1}u_i^*$ using the previous time-step value, as

$$\frac{(\rho^{n+1}u_i^*)_p - (\rho^n u_i^n)_p}{\Delta t} V_{cv} = -\left[\sum_{f_k} \langle u_{i,p}\rangle_{p\to f_k} (RU)_{f_k} - \sum_{f_k} \langle u_{i,p}\rangle_{p\to f_k} (\vec{f}\cdot\vec{n})_f\right]^n A_{f_k}. \tag{2.11}$$

2.4.3. *Face flux update*

It is well known that a collocated formulation leads to the velocity/pressure decoupling, which results in a pressure checkerboard issue. To avoid this issue in the pressure field, we perform Rhie-Chow-like interpolation with a balanced-force approach when updating the face flux as

$$(RU)^{**}_{f_k} = \langle(\rho^{n+1}u_i^*)_p\rangle_{p\to f_k} n_{i,f} + \Delta t\left[-\left(\frac{\partial p}{\partial n}\right)^n_f + \left(\vec{F}_f\cdot\vec{n}_{f_k}\right)^{n+1}\right], \tag{2.12}$$

where the variables with a superscript $**$ indicate another set of intermediate variables.

2.4.4. *Pressure Poisson solve*

After solving Eq. (2.11) and Eq. (2.12), the intermediate mass flux at the cell faces contains the contributions from convection terms, the pressure gradient at time step n, and other body forces, such as surface tension and gravity force. At this point, the intermediate velocity $U^{**}_{f_k}$ from the face flux $(RU)^{**}_{f_k}$ does not necessarily satisfy the divergence-free condition. To update the velocity (Eqs. (2.15)–(2.16)), we first solve the pressure Poisson equation to compute the correction pressure δp (see Eq. (2.14) for the definition of δp). The pressure Poisson equation is given as

$$\sum_{f_k} U^{**}_{f_k} A_{f_k} = -\Delta t \sum_{f_k} \frac{1}{\langle\rho_p^{n+1}\rangle_{p\to f_k}} \left(\frac{\partial \delta p}{\partial n}\right)^{n+1}_f A_{f_k}, \tag{2.13}$$

where $U^{**}_{f_k} = (RU)^{**}_{f_k}/\langle\rho_p^{n+1}\rangle_{p\to f}$. Solving Eq. (2.13), we obtain the correction pressure at the cell center δp_p.

2.4.5. *Pressure update*

Next, the pressure is updated using the correction pressure to obtain the cell center pressure at time step $n+1$, as

$$p_p^{n+1} = p_p^n + \delta p_p^{n+1}. \tag{2.14}$$

2.4.6. *Cell velocity update*

The pressure gradient and body force at time step $n+1$ are added to the cell velocity to obtain an approximately divergence-free velocity field at the cell center, as velocity at the cell center $u_{i,p}$ is updated with the updated pressure p^{n+1} as

$$u_{i,p}^{n+1} = u_{i,p}^* + \frac{\Delta t}{\rho_p^{n+1}}\left[-\left(\frac{\partial p}{\partial x_i}\right)^{n+1}_p + \vec{F}_p^{n+1}\right]. \tag{2.15}$$

Note that $u_{i,p}$ is approximately divergence-free condition since the pressure Poisson equation is solved at cell faces with $U^{**}_{f_k}$. We emphasize that the pressure gradient and the

additional forces here are computed at the cell center using the least-square gradient operator that uses the values at cell faces. This is done to enforce a discrete balance between the pressure gradient and other forces even at the cell center.

2.4.7. *Face velocity/flux update*

Finally, the face flux is updated such that the velocity at the face exactly satisfies the divergence-free condition, as

$$(RU)_{f_k}^{n+1} = (RU)_{f_k}^{**} + \Delta t \left[- \left(\frac{\partial \delta p}{\partial n} \right)_f^{n+1} \right]. \tag{2.16}$$

The updated face flux is saved to be used in the next substep/timestep in Eqs. (2.10)–(2.11).

3. Results

In this section, we present the simulation results of the ACDI method on the Voronoi unstructured grid. We use canonical test cases in addition to new test cases that we designed to systematically evaluate interface-capturing methods on unstructured grids. Advection of a single drop with initially uniform velocity fields, a drop in a vortex, and homogeneous isotropic turbulence (HIT) are used as the test cases. We investigate the accuracy of the method, boundedness of the PF variable ϕ, total volume (mass) conservation, and robustness of the method using kinetic energy change. As a metric for an accurate interface advection, we define the shape error as

$$\mathcal{E} = \sum_{cv} |\phi_{cv} - \phi_{0,cv}| dV_{cv}^{\frac{2}{3}}, \tag{3.1}$$

where ϕ_0 denotes the initial PF field at $t = 0$.

For all the simulations, Γ and ϵ are chosen as $\Gamma = 1.0 \times |u_{max}|$ and $\epsilon = 0.6 \times \Delta x_{max}$, where $|u_{max}|$ is the maximum velocity in the flow field and Δx_{max} is the maximum grid size in the domain. The time-step size is fixed as $\Delta t = 0.001$.

3.1. *Drop advection*

For the advection test case, we consider a two-dimensional unit square domain $[0.0, 1.0] \times [0.0, 1.0]$ with a drop of radius $r = 0.15$ initially located at the center $(x, y) = (0.5, 0.5)$. Simulations are initialized with a uniform velocity field $(u, v) = (1.0, 0.0)$ and run until $t = 4$, which is 4 periods of drop advection. The ACDI model in Eq. (2.1) is coupled with the consistent momentum equation in Eq. (2.6). We consider four different grids as described below to fully evaluate the accuracy of the method in various situations, such as interface advection through and along grid transitions and domains with partially refined regions. These test cases are important because the accuracy of a phase-field method is dependent on the truncation error in the numerical scheme used, which is locally a function of the grid topology.

The four grids we consider are as follows.

(*a*) A uniform grid of 128×128.

(*b*) A base grid of 64×64 with refinement in the region of $y \in [0.3, 0.7]$ by a factor of 4. The drop is fully inside the refined region in this case.

(*c*) A base grid of 64×64 with refinement in the region of $x \in [0.48, 0.52]$ by a factor of 4. The drop advection direction is parallel to the gradient of grid transition, so the drop passes through the grid transition region once for each period of advection.

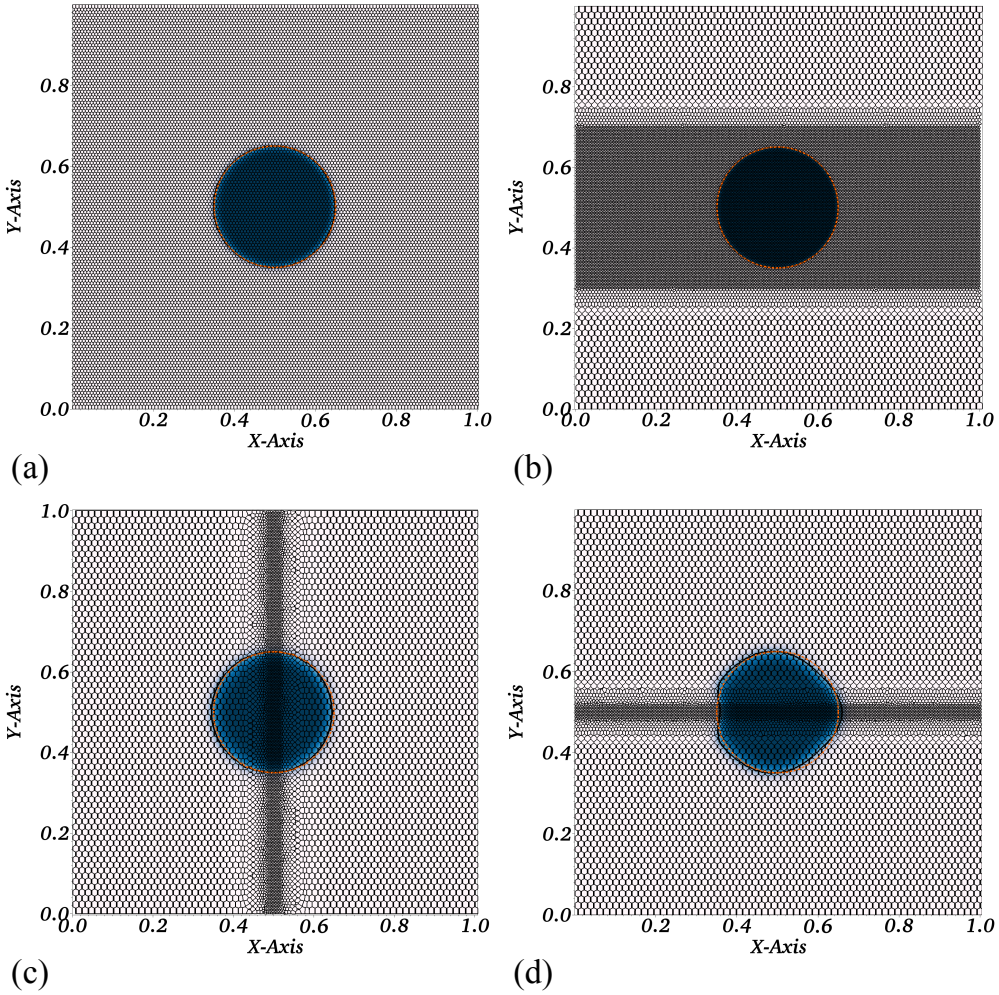

FIGURE 2. Snapshots of ϕ field for the advection test cases at the final time of $t = 4$. The orange solid line shows the initial drop. Blue and white indicate ϕ values of unity and zero, respectively. Black solid lines represent the mesh.

(d) A base grid of 64×64 with refinement in the region of $y \in [0.48, 0.52]$ by a factor of 4. The drop advection direction is perpendicular to the gradient of grid transition, so the drop is always in the grid transition region.

The results from the droplet advection case are shown in Figure 2 at the final time of $t = 4$. The shape error (Eq. (3.1)) for each case is (a) $\mathcal{E} = 8.326 \times 10^{-4}$, (b) $\mathcal{E} = 4.563 \times 10^{-4}$, (c) $\mathcal{E} = 2.374 \times 10^{-3}$, and (d) $\mathcal{E} = 5.015 \times 10^{-3}$. We confirm that the conservation of the total volume and the boundedness of ϕ for all cases. For cases (c) and (d), the shape error accumulates faster compared to other cases as the droplet encounters regions of grid transition. The shape error for case (c) is better than case (d) because the drop encounters the grid transition only once per period of advection, as opposed to advection always being along the grid transition. This suggests that the present method results in accurate simulations of two-phase flows in realistic simulations of engineering

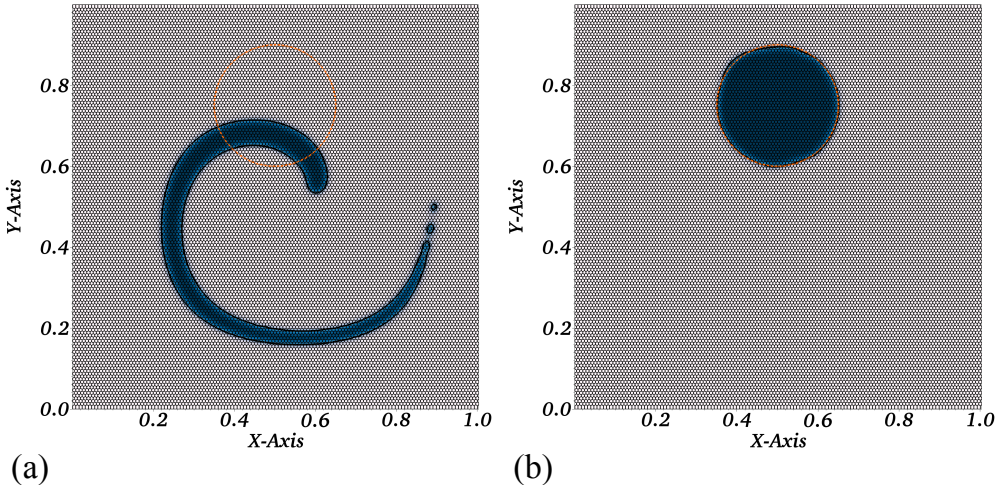

FIGURE 3. Snapshots of ϕ field of vortex-in-a-box test case. The orange solid line shows the initial drop. Blue and white indicate ϕ values of unity and zero, respectively, at time (a) $t = 2$ and (b) $t = 4$. The black solid line represents the mesh.

interest, where one would typically use complex meshes with grid transitions. For cases (a) and (b), where the drop does not encounter grid transition regions, the shape error is sufficiently low and the initial drop shape is maintained.

3.2. *Drop in a vortex*

In this section, we evaluate the method using a drop-in-a-vortex case where the drop undergoes shearing deformation. We consider a two-dimensional unit square domain $[0.0, 1.0] \times [0.0, 1.0]$ with a uniform HCP mesh of size 128×128. Initially, a drop of radius $r = 0.15$ is placed at $(x, y) = (0.5, 0.75)$. Here, the ACDI method [Eq. (2.1)] is decoupled from the momentum equation (Eq. (2.6)), and instead a velocity field of

$$u = -\sin^2(\pi x)\sin(2\pi y)\cos\left(\frac{\pi t}{T}\right), \tag{3.2}$$

$$v = \sin(2\pi x)\sin^2(\pi y)\cos\left(\frac{\pi t}{T}\right), \tag{3.3}$$

is prescribed at every time step. Here, the period T is set as $T = 4$.

Results from this simulation (Figure 3) show the droplet shapes at a half-time of $t = 2$ and a final time of $t = 4$. The drop undergoes deformation until $t = 2$, and the flow field is reversed to recover the initial drop shape at $t = 4$. Figure 3 shows that the method accurately recovers the final circular shape of the drop on an HCP mesh. The total volume is discretely conserved throughout the simulation, and we confirm the boundedness of ϕ. The shape error at the final time is $\mathcal{E} = 1.903 \times 10^{-3}$.

3.3. *Drop in HIT field*

In this section, we perform an infinite Reynolds number simulation of a drop in isotropic turbulence. This test case is useful to evaluate the robustness of the method. For a stable method, the kinetic energy either remains constant or decays with time. A triply periodic cubic box of size $[0, 2\pi] \times [0, 2\pi] \times [0, 2\pi]$ is considered as the simulation domain. The

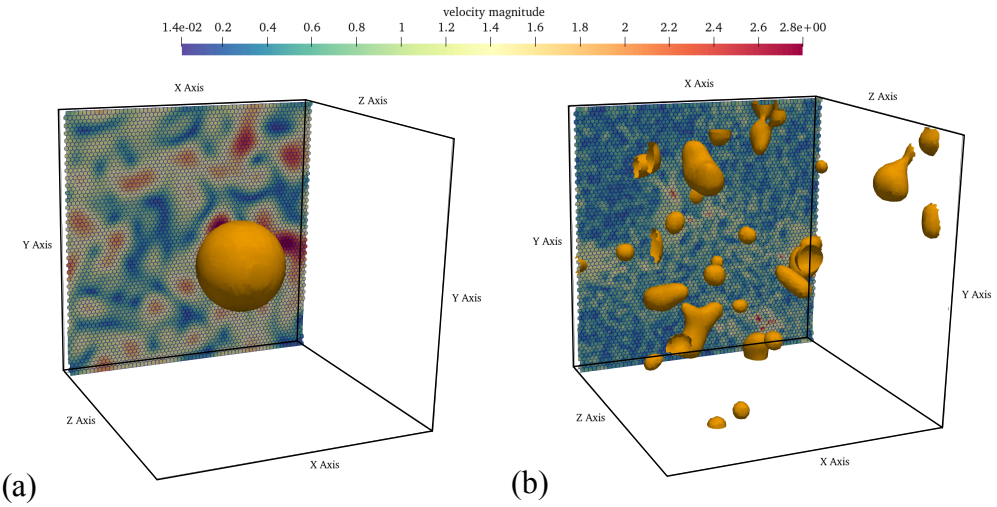

FIGURE 4. Snapshots of the drop-laden HIT simulations at (a) $t = 0$ and (b) $t = 8$. The iso-surface indicates the contour of PF variable with $\phi = 0.5$.

initial velocity field is set following the model energy spectrum from Passot & Pouquet (1987) as

$$E(k) \propto k^4 \exp\left[-2\left(\frac{k}{k_0}\right)^2\right], \tag{3.4}$$

where k is the wavenumber and $k_0 = 4$ is the most energetic wavenumber. A spherical drop of radius $r = 1.0$ is initially placed at the center of the domain. The dynamic viscosity of the two fluids is chosen to be zero for the infinite Reynolds number case, and the surface tension is set to zero. The simulation is repeated with different density ratios $\rho_1/\rho_2 = 1$, 10, 100, and 1000.

The inviscid simulations are run until $t = 8$, and we track total kinetic energy, defined as

$$K = \sum_{cv} \rho u_{i,cv} u_{i,cv} dV_{cv}. \tag{3.5}$$

The iso-surface of the PF variable at $\phi = 0.5$ is illustrated in Figure 4 at $t = 0$ and $t = 8$. Throughout the simulations, the total volume is perfectly conserved, while the PF variable is bounded. The ratio of the total kinetic energy to its initial value K/K_0 is plotted in Figure 5 from $t = 0$ to $t = 3$. Since no dissipation mechanisms are present, the ratio of the total kinetic energy is expected to be conserved as unity. However, we observe the decay of kinetic energy for all the density ratio cases. As a comparison, we plot results from two additional cases with a fully compressible single-phase ideal-gas solver (Lakebrink *et al.* 2019) and a low-Mach single-phase Helmholtz solver (Ambo *et al.* 2020) that use different methods for the projection step. For the low-Mach and fully compressible flow cases, the Mach number is set to $Ma < 0.05$ to ensure incompressibility of the flow. As shown in Figure 5, the ideal-gas solver almost preserves the kinetic energy, but it shows mild decay of the total kinetic energy. On the other hand, the Helmholtz solver shows behavior similar to that of the present method, with a faster decay of the total kinetic energy after $t \approx 1.0$. But the dissipative nature of the error in total kinetic energy ensures that all the methods are numerically stable.

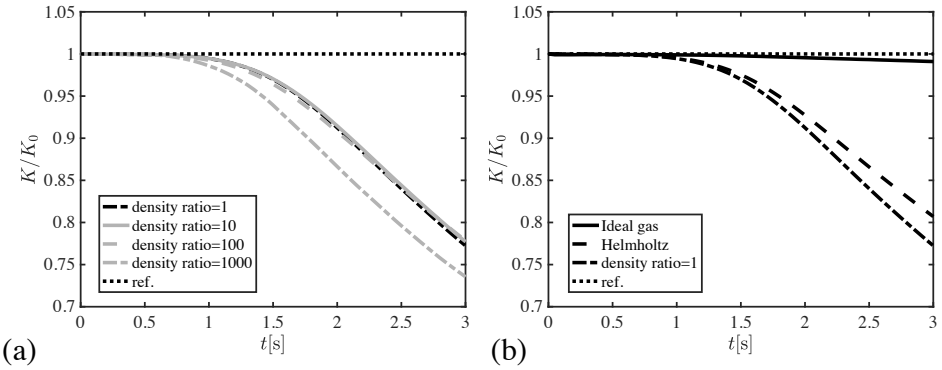

FIGURE 5. Kinetic energy ratio for the HIT setup in Section 3.3: (a) with different density ratios and (b) with different solvers. Lines denote the kinetic energy ratio with different density ratios and different solvers: black solid, ideal-gas solver; black dashed, Helmholtz solver; black dash-dotted, $\rho_1/\rho_2 = 1$; gray solid, $\rho_1/\rho_2 = 10$; gray dashed, $\rho_1/\rho_2 = 100$; and gray dash-dotted, $\rho_1/\rho_2 = 1000$. The black-dotted line shows a constant unity line for reference.

4. Conclusions

In this work, a phase-field method is presented for the simulation of two-phase flows on unstructured grids. We adopt the ACDI method recently proposed by Jain (2022) and present a formulation for the Voronoi-mesh-based unstructured grid. The Voronoi grid is chosen in this study because of its many attractive features, such as uniquely defined connectivity, suitability for the use of less-dissipative central schemes, and highly parallelizable mesh generation. Because the ACDI method is significantly more accurate than other existing phase-field methods, its application to Voronoi-grid-based unstructured grids has great potential to be an effective interface-capturing method for the simulation of two-phase flows in realistic engineering applications.

In this work, in addition to the use of canonical test cases, we also designed new test cases to fully evaluate the performance of interface-capturing methods on unstructured grids with grid transitions. We used these cases to evaluate the accuracy of the proposed method and showed that the proposed method is accurate and is suitable to be used for accurate numerical simulations with unstructured grids on complex domains of engineering interest that will involve grid transitions. In all the simulations, we confirmed that the volume fraction was bounded without any clipping or the use of flux limiter. Moreover, the total volume (mass) was discretely conserved.

We also performed droplet-laden HIT simulations at infinite Reynolds number to evaluate the robustness of the method for turbulent flow simulations. The proposed method is found to be stable for all the density ratios considered due to the use of consistent momentum equations (Eqs. (2.1)–(2.6)). The total kinetic energy was found to decrease with time for all the density ratio cases, due to the use of a fractional-step projection method to enforce a divergence-free condition with a collocated-grid formulation.

Acknowledgments

This study was supported by funding from the National Science Foundation under grant CMMI-21311961 (to H. H.) and Boeing Co. (to S. S. J.).

REFERENCES

Allen, S. M. & Cahn, J. W. 1979 A microscopic theory for antiphase boundary motion and its application to antiphase domain coarsening. *Acta metallurgica* **27**(6), 1085–1095.

Ambo, K., Nagaoka, H., Philips, D. A., Ivey, C., Brès, G. A., & Bose, S. T. 2020 Aerodynamic force prediction of the laminar to turbulent flow transition around the front bumper of the vehicle using dynamic-slip wall model LES. *AIAA Paper 0036*.

Brackbill, J. U., Kothe, D. B., & Zemach, C. 1992 A continuum method for modeling surface tension. *J. Comput. Phys.* **100**(2), 335–354.

Brès, G. A., Bose, S. T., Emory, M., Ham, F., Schmidt, O. T., Rigas, G., & Colonius, T. 2018 Large-eddy simulations of co-annular turbulent jet using a Voronoi-based mesh generation framework. *AIAA Paper 3302*.

Buckley, M. P. & Veron, F. 2016 Structure of the airflow above surface waves. *J. Phys. Oceanogr.* **46**(5), 1377–1397.

Cahn, J. W. & Hilliard, J. E. 1958 Free energy of a nonuniform system. I. Interfacial free energy. *Chem. Phys.* **28**(2), 258–267.

Chiapolino, A., Saurel, R. & Nkonga, B. 2017 Sharpening diffuse interfaces with compressible fluids on unstructured meshes. *J. Comput. Phys.* **340**, 389–417.

Chiu, P.-H. & Lin, Y.-T. 2011 A conservative phase field method for solving incompressible two-phase flows. *J. Comput. Phys.* **230**(1), 185–204.

Gorokhovski, M. & Herrmann, M. 2008 Modeling primary atomization. *Annu. Rev. Fluid Mech.* **40**, 343–366.

Holmes, R. L., Dimonte, G., Fryxell, B., Gittings, M. L., Grove, J. W., Schneider, M., Sharp, D. H., Velikovich, A. L., Weaver, R. P., & Zhang, Q. 1999 Richtmyer–Meshkov instability growth: experiment, simulation and theory. *J. Fluid Mech.* **389**, 55–79.

Hwang, H., Chan, W. H. R., Jain, S. S., & Abarzhi, S. I. 2021 Scale-dependent Rayleigh–Taylor dynamics with variable acceleration in a finite-sized domain for three-dimensional flows. *Phys. Fluids* **33**(9), 092108.

Hwang, H., Kim, D., & Moin, P. 2022 Atomization of the optimally disturbed liquid jets. *Phys. Rev. Fluids* **7**(11), 110508.

Ivey, C. B. & Moin, P. 2015 Accurate interface normal and curvature estimates on three-dimensional unstructured non-convex polyhedral meshes. *J. Comput. Phys.* **300**, 365–386.

Ivey, C. B. & Moin, P. 2017 Conservative and bounded volume-of-fluid advection on unstructured grids. *J. Comput. Phys.* **350**, 387–419.

Jain, S. S. 2022 Accurate conservative phase-field method for simulation of two-phase flows. *J. Comput. Phys.* **469**, 111529.

Jain, S. S. & Moin, P. 2022 A kinetic energy–and entropy-preserving scheme for compressible two-phase flows. *J. Comput. Phys.*, 111307.

Jain, S. S., Tyagi, N., Prakash, R. S., Ravikrishna, R., & Tomar, G. 2019 Secondary breakup of drops at moderate Weber numbers: effect of density ratio and Reynolds number. *Int. J. Multiphase Flow* **117**, 25–41.

Jofre, L., Borrell, R., Lehmkuhl, O., & Oliva, A. 2015 Parallel load balancing strategy for volume-of-fluid methods on 3-D unstructured meshes. *J. Comput. Phys.* **282**, 269–288.

Joshi, V. & Jaiman, R. K. 2018 An adaptive variational procedure for the conservative and positivity preserving Allen–Cahn phase-field model. *J. Comput. Phys.* **366**, 478–504.

Kim, D., Ivey, C. B., Ham, F. E., & Bravo, L. G. 2021 An efficient high-resolution volume-of-fluid method with low numerical diffusion on unstructured grids. *J. Comput. Phys.* **446**, 110606.

Kumar, R., Cheng, L., Xiong, Y., Xie, B., Abgrall, R., & Xiao, F. 2021 THINC scaling method that bridges VOF and level set schemes. *J. Comput. Phys.* **436**, 110323.

Lafaurie, B., Nardone, C., Scardovelli, R., Zaleski, S., & Zanetti, G. 1994 Modelling merging and fragmentation in multiphase flows with surfer. *J. Comput. Phys.* **113**(1), 134–147.

Lakebrink, M. T., Mani, M., Rolfe, E. N., Spyropoulos, J. T., Philips, D. A., Bose, S. T. & Mace, J. L. 2019 Toward improved turbulence-modeling techniques for internal-flow applications. *AIAA Paper 3703*.

Liu, H., Chen, H., Cai, C., Jia, M., & Yin, H. 2019 Numerical investigation on the unsteady spray cooling of high temperature steel plate. *Int. J. Heat Mass Transf.* **143**, 118342.

Mahesh, K., Constantinescu, G., & Moin, P. 2004 A numerical method for large-eddy simulation in complex geometries. *J. Comput. Phys.* **197**(1), 215–240.

Mirjalili, S., Jain, S. S., & Dodd, M. 2017 Interface-capturing methods for two-phase flows: An overview and recent developments. *Annual Research Briefs*, Center for Turbulence Research, Stanford University, 117–135.

Passot, T. & Pouquet, A. 1987 Numerical simulation of compressible homogeneous flows in the turbulent regime. *J. Fluid Mech.* **181**, 441–466.

Perot, B. 2000 Conservation properties of unstructured staggered mesh schemes. *J. Comput. Phys.* **159**(1), 58–89.

Prakash, S. R., Jain, S. S., Lovett, J. A., Raghunandan, B., Ravikrishna, R., & Tomar, G. 2019 Detailed numerical simulations of atomization of a liquid jet in a swirling gas crossflow. *At. Sprays* **29**(7).

Rider, W. J. & Kothe, D. B. 1998 Reconstructing volume tracking. *J. Comput. Phys.* **141**(2), 112–152.

Sharp, D. H. 1984 An overview of Rayleigh–Taylor instability. *Phys. D: Nonlinear Phenom.* **12**(1–3), 3–18.

Sui, Y., Ding, H., & Spelt, P. D. 2014 Numerical simulations of flows with moving contact lines. *Annu. Rev. Fluid Mech.* **46**, 97–119.

Tryggvason, G., Esmaeeli, A., & Al-Rawahi, N. 2005 Direct numerical simulations of flows with phase change. *Comput. Struct.* **83**(6–7), 445–453.

Xiao, F., Honma, Y., & Kono, T. 2005 A simple algebraic interface capturing scheme using hyperbolic tangent function. *Int. J. Numer. Methods Fluids* **48**(9), 1023–1040.

Xie, B. & Xiao, F. 2017 Toward efficient and accurate interface capturing on arbitrary hybrid unstructured grids: the THINC method with quadratic surface representation and gaussian quadrature. *J. Comput. Phys.* **349**, 415–440.

Youngs, D. L. 1982 Time-dependent multi-material flow with large fluid distortion. *Numerical methods for fluid dynamics*.